

Modeling the Metal–Insulator Phase Transition in Li_xCoO_2 for Energy and Information Storage

Neel Nadkarni, Tingtao Zhou, Dimitrios Fraggedakis, Tao Gao, and Martin Z. Bazant*

An electro-chemomechanical phase-field model is developed to capture the metal–insulator phase transformation along with the structural and chemical changes that occur in Li_xCoO_2 in the regular operating range of $0.5 < x < 1$. Under equilibrium, in the regime of phase coexistence, it is found that transport limitations lead to kinetically arrested states that are not determined by strain-energy minimization. Further, lithiation profiles are obtained for different discharging rates and the experimentally observed voltage plateau is observed. Finally, a simple model is developed to account for the conductivity changes for a polycrystalline Li_xCoO_2 thin film as it transforms from the metallic phase to the insulating phase and a strategy is outlined for memristor design. The theory can therefore be used for modeling Li_xCoO_2 -electrode batteries as well as low voltage nonvolatile redox transistors for neuromorphic computing architectures.

1. Introduction

Li_xCoO_2 (LCO) has been one of the most successful cathode materials used in conventional Li-ion batteries^[1,2] since 1980s.^[3,4] LCO has unique structural and material properties that change as the material undergoes lithiation/delithiation. Extensive *ab initio*^[5–12] and experimental investigations^[13–25] have been performed to characterize LCO properties at different lithium content under equilibrium and nonequilibrium conditions. For concentrations in the range of $0.5 < x < 1$, LCO, belonging to the $R\bar{3}m$ space group, has a hexagonal closed-pack structure with rhombohedral symmetry.^[8,12] At $x = 0.5$, the lattice undergoes an irreversible order–disorder phase transition with a large expansion of the c parameter of the lattice.^[13,15,17] Hence, for reversible cyclability, the concentration of the lithium is constrained in the range of $0.5 < x < 1$.^[12,13] During

the lithiation process, the crystal structure of LCO remains unchanged with the host lattice contracting along the c -axis.^[8,12,13]

Another important characteristic of LCO is the metal–insulator transition, in which the material transitions from a good ($x < 0.75$) to a poor ($x > 0.94$) electron conductor.^[8,21,25] The metal–insulator phase coexistence, during the transition, is observed macroscopically through a voltage plateau in the voltage versus state of charge diagram, occurring over the entire range of $0.75 < x < 0.94$.^[13,21,25] The layered structure of LCO allows for Li to diffuse only in the plane perpendicular to the [0001] direction, leading to effectively 2D transport in the crystal.^[11,26] LCO is therefore a widely studied material and

has been in commercial use in battery technology for over three decades.^[1,2] Thus, developing a predictive mesoscopic model is paramount in studying the nonequilibrium charging/discharging as well as phase-separating behavior for this material.

Recently, there has been renewed interest in LCO because of its metal–insulator transition behavior for the development of nonvolatile redox memristors to be used in neuromorphic computing technology.^[27] In order to mimic the efficiency of the human brain, neuromorphic computing architecture is becoming an exciting avenue toward development of hardware specialized for machine learning and pattern recognition algorithms.^[28–30] Current CMOS technologies consume high energy due to the movement of data between the processor, and static and dynamic random access memory.^[27,31] In contrast, resistive memory crossbars, in which processing and memory storage occurs simultaneously, have been predicted to lower this energy requirement by six orders of magnitude.^[32,33]

The memristor, first proposed by Leon Chua, is the unit circuit element that forms the basis of this architecture.^[34] The current state-of-the-art memristors, e.g., phase-change memories (PCM)^[35–37] or filamentary-type metal oxide memories,^[38,39] face drawbacks such as stochasticity in state switching (high “write” noise)^[40] and “write” nonlinearities^[41] as well as large switching voltages and currents.^[36,42] To overcome some of these challenges, all solid-state intercalation devices that use Li-ion/proton intercalation^[27,43–46] have been proposed as alternative memristor candidates. These devices require low power for switching and maintain their resistive state over large periods of time, i.e., are nonvolatile, as the dopants (intercalated ions) cannot diffuse out of the system without applying an external bias voltage.^[27,43]

Dr. N. Nadkarni, D. Fraggedakis, Dr. T. Gao, Prof. M. Z. Bazant

Department of Chemical Engineering
Massachusetts Institute of Technology
Cambridge, MA 02139, USA

E-mail: bazant@mit.edu

T. Zhou

Department of Physics
Massachusetts Institute of Technology
Cambridge, MA 02139, USA

Prof. M. Z. Bazant

Department of Mathematics
Massachusetts Institute of Technology
Cambridge, MA 02139, USA

 The ORCID identification number(s) for the author(s) of this article can be found under <https://doi.org/10.1002/adfm.201902821>.

DOI: 10.1002/adfm.201902821

Fuller et al.^[27] recently demonstrated this concept by designing a Li-ion synaptic transistor (LISTA) which makes use of the metal–insulator transition zone in LCO. During the process of this transition, the conductivity of the material was shown to change by six orders of magnitude.^[25] The metal–insulator transition property of LCO can therefore be used to tune the resistivity as a function of the state of charge (or Li concentration) stored in the material. Hence, modeling this behavior is key in the computational design of these redox memristive devices for future computing platforms along with modeling of current battery technology. Additionally, the integration of neuromorphic computing architecture in flexible bioelectronic circuits makes it essential to model their response under large deformations.^[43] Previous studies on modeling LCO have not included the thermodynamics of the material in consistent fashion and have also ignored the metal–insulator coexistence region altogether.^[47–50]

The main goals of this paper are to i) develop an electro-chemomechanical model that accounts for the two-phase coexistence in the metal–insulator transition region, lattice expansions, and intercalation stresses due to lithium ion insertion, and thermodynamically consistent intercalation reaction kinetics in single crystalline LCO nanoparticles; ii) model the conductivity changes due to the metal–insulator transition in a polycrystalline nanoscale thin film used in LCO-based memristor devices such as LISTA. Our theory is based on the phase-field modeling technique, which has proved to be successful for other battery materials such as Li_xFePO_4 ,^[51–53] Li_xTiO_2 ,^[54] $\text{Li}_{4+x}\text{Ti}_5\text{O}_{12}$,^[55] among others. We present our theoretical model and numerical results for static phase boundary orientations under equilibrium as well as nonequilibrium voltage curves for different values of applied current that predict the existence of voltage plateaus in the metal–insulator coexisting region, according to the Maxwell construction and in agreement with porous electrode experiments. We envision that this model can be used for device-level simulations of Li_xCoO_2 -based low voltage memristors as well as porous electrode battery simulations.^[56,57]

2. Theoretical Model

We propose a mesoscopic electro-chemomechanical continuum phase field model for Li_xCoO_2 , where the free energy for a single crystal is given by

$$G[\mathbf{u}, x] = \int_V \left\{ g_h(x) + \frac{1}{2} \kappa |\nabla x|^2 + \frac{1}{2} (\boldsymbol{\varepsilon} - \boldsymbol{\varepsilon}_0(x)) : \mathbb{C} (\boldsymbol{\varepsilon} - \boldsymbol{\varepsilon}_0(x)) \right\} dV \quad (1)$$

In this model, x is the concentration of Li ions scaled with the maximum theoretical capacity x_{\max} in Li_xCoO_2 , and \mathbf{u} is the displacement field in the particle. $g_h(x)$ is the homogeneous free energy of the system that includes entropic and enthalpic effects. The second term in the free energy represents the gradient penalty or the required to form an interface when phase separation occurs. The last term denotes the mechanical free energy of the system where $\boldsymbol{\varepsilon}$ is the strain in the material at each point and $\boldsymbol{\varepsilon}_0(x)$ is the lattice expansion caused due to accumulation of lithium. The tensor \mathbb{C} represents the elastic

modulus of the material. Similar models have been used in modeling other phase-separating intercalation materials.^[51–53,58]

The homogeneous free energy of the material is obtained from experiments performed by Reynier et al., on Li_xCoO_2 coin cells.^[59] The equilibrium concentrations along which phase separation occurs have been estimated to be $0.75 < x < 0.94$.^[8,21,25] We determine the theoretical homogeneous chemical potential by fitting the experiments with a Redlich–Kister equation^[60]

$$g_h(x)/x_{\max} = \mu^\theta x + RT \left[x \log x + (1-x) \log(1-x) \right] + x(1-x) \sum_{k=1}^N \Omega_k (1-2x)^{k-1} \quad (2)$$

such that the chemical potential values are tuned to match at $x_1 \approx 0.75$ and $x_2 \approx 0.94$. We obtain a good fit with the experimental free energy curve of the curves with only three parameters ($N=3$). This ensures that the phase separation occurs at these two concentrations with the Maxwell line given by

$$\mu_h(x_1) = \mu_h(x_2) = \frac{g_h(x_2) - g_h(x_1)}{x_2 - x_1} \quad (3)$$

where $\mu_h(x) = g'(x)$ is the homogenous chemical potential.

A schematic of the structure is shown in **Figure 1**. Li_xCoO_2 is a layered transition metal oxide material with a hexagonal closed packing structure characterized by the inplane lattice parameter a and depth lattice parameter c . As lithiation proceeds, the lattice parameter contracts along the c -axis, as observed in experiment and first-principles calculations, with small changes in the in-plane a -axis lattice parameter.^[8,12] As reference for measuring the strain we choose the lattice state at $x = 0.5$. Therefore, the lattice misfit strain $\boldsymbol{\varepsilon}_0(x)$ in the regular cartesian basis has the form

$$\boldsymbol{\varepsilon}_0(x) = \begin{bmatrix} \varepsilon_a(x) & 0 & 0 \\ 0 & \varepsilon_a(x) & 0 \\ 0 & 0 & \varepsilon_c(x) \end{bmatrix} \quad (4)$$

The variation in the lattice parameter along the a -axis is much smaller than that along the c -axis, $\varepsilon_a \ll \varepsilon_c$, and hence is neglected. The functional form of the misfit strain in the c -axis $\varepsilon_c(x)$ is obtained through fitting with experimental values,^[13]

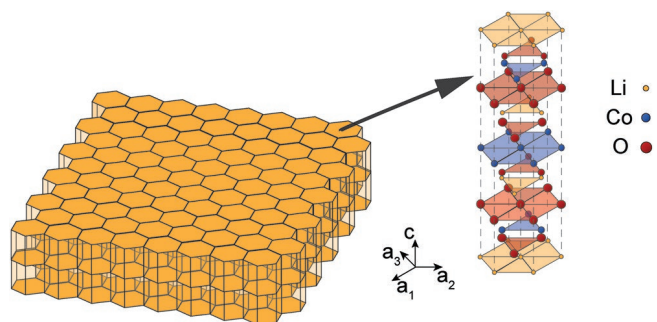


Figure 1. The lattice of hexagonal-closed-packed (hcp) layers forming a nanoparticle that we analyze for our model. The layered structure is a repeated periodic arrangement of lithium, cobalt and oxygen atoms.

which are in agreement with first principles theoretical predictions.^[12] The elastic stiffness tensor is obtained from ab initio calculations.^[50] We further assume that mechanical relaxation occurs at a much faster rate than ion transport and insertion, and hence the system is assumed to be in mechanical equilibrium while being chemically out of equilibrium. The mechanical governing equations for the system are acquired through the minimization of the free energy with respect to the displacements, providing us with

$$\nabla \cdot \boldsymbol{\sigma} = 0 \quad (5)$$

where $\boldsymbol{\sigma}$ is the stress field in the medium, given by the constitutive relation

$$\boldsymbol{\sigma} = \mathbb{C} : [\boldsymbol{\varepsilon} - \boldsymbol{\varepsilon}_0(x)] \quad (6)$$

As there are no external tractions applied to the particle, the boundary condition for the mechanical equation is

$$\boldsymbol{\sigma} \cdot \mathbf{n} = \mathbf{0} \quad (7)$$

Next, minimizing the free energy with respect to the concentrations provides the electro-chemomechanical potential

$$\mu = \frac{\delta G}{\delta x} = g'(x) - \kappa \nabla^2 x - x_{\max}^{-1} \boldsymbol{\sigma} : \boldsymbol{\varepsilon}'_0(x) \quad (8)$$

The ion transport occurs through diffusion of the ions in the ab plane and the diffusive flux \mathbf{j} is given by

$$\mathbf{j} = -\frac{D(x)}{RT} \nabla \mu \quad (9)$$

where $D(x)$ is the concentration-dependent diffusivity. In the ab initio simulations by Van der Ven and Ceder,^[26] the diffusion in Li_xCoO_2 was proposed to occur only through two 2D pathways, namely i) the tetrahedral site hop (TSH), or ii) the oxygen dumbbell hop (ODH). In the TSH, the diffusion occurs through an isotropic basal in-plane divacancy migration. In contrast, the diffusion in the ODH occurs through Li squeezing in between two oxygen atoms. However, due to the activation energy of ODH being significantly higher than the TSH mechanism, the transition of ion migration to ODH occurs only at infinite vacancy dilutions (i.e., $x \approx 1$). The diffusivity in our model is taken from ref. [26]. The concentration in the particle evolves according to the conservation equation

$$\frac{\partial x}{\partial t} + \nabla \cdot \mathbf{j} = 0 \quad (10)$$

with the natural boundary condition for the surface

$$\mathbf{n} \cdot (\kappa \nabla x) = 0 \quad (11)$$

The ion insertion process occur at the boundaries of the nanoparticle and is modeled through a charge-transfer reaction^[61] given by

$$\mathbf{j} \cdot \mathbf{n} = R(x, \mu, \phi) \quad (12)$$

where ϕ is the battery voltage or the difference between the electrostatic potentials of the electrode and electrolyte. The reaction



is modeled using the nonequilibrium thermodynamics framework described in ref. [61] where

$$R(c, \mu, \phi) = k_0 \frac{(a_{\text{O}} a_{\text{e}})^{1-\alpha} (a_{\text{R}})^{\alpha}}{\gamma_{\ddagger}} \left[\exp\left(-\alpha \frac{F\eta}{RT}\right) - \exp\left((1-\alpha) \frac{F\eta}{RT}\right) \right] \quad (14)$$

The quantities a_{O} , a_{e} , and a_{R} are the activities of the oxidized, electrons, and reduced species, respectively, while γ_{\ddagger} is the activity coefficient of the transition state and depends upon the concentration of vacancies as $\gamma_{\ddagger} = (1-x)^{-1}$. The charge transfer coefficient is denoted with α . The overpotential of the reaction η is defined as

$$\eta = \frac{\mu - F\phi}{F} \quad (15)$$

Additionally, we model galvanostatic operational conditions (constant current) by enforcing the following equation

$$F \int_{A_{\text{reac}}} \mathbf{j} \cdot \mathbf{n} \, dA = I \quad (16)$$

where I is the applied current, F is the Faraday constant, and A_{reac} corresponds to the reactive area. The faces perpendicular to the c -axis are impenetrable to the flux of Li ions, and hence all faces except the ones normal to the c -axis are taken to be the reacting ones. Equation (16) closes the system to obtain the battery voltage ϕ as a function of the state of charge. A finite element discretization is used to numerically solve for the solutions of these equations.^[62] The parameters used in our simulations are provided in the Supporting Information.

3. Results

3.1. Relaxation Simulations and Kinetically Arrested Equilibrium States

Theoretically, the equilibrium configuration of the system will correspond to the state that minimizes the free energy of the particle, subject to the discussed boundary conditions. If the average Li concentration in the particle lies in $0.75 < x < 0.94$, the minimization of the chemical free energy will force the system to phase separate into the two equilibrium concentrations $x_1 \approx 0.75$ and $x_2 \approx 0.94$, with volume fractions

$$v_1 = \frac{x_2 - x}{x_2 - x_1} \quad (17)$$

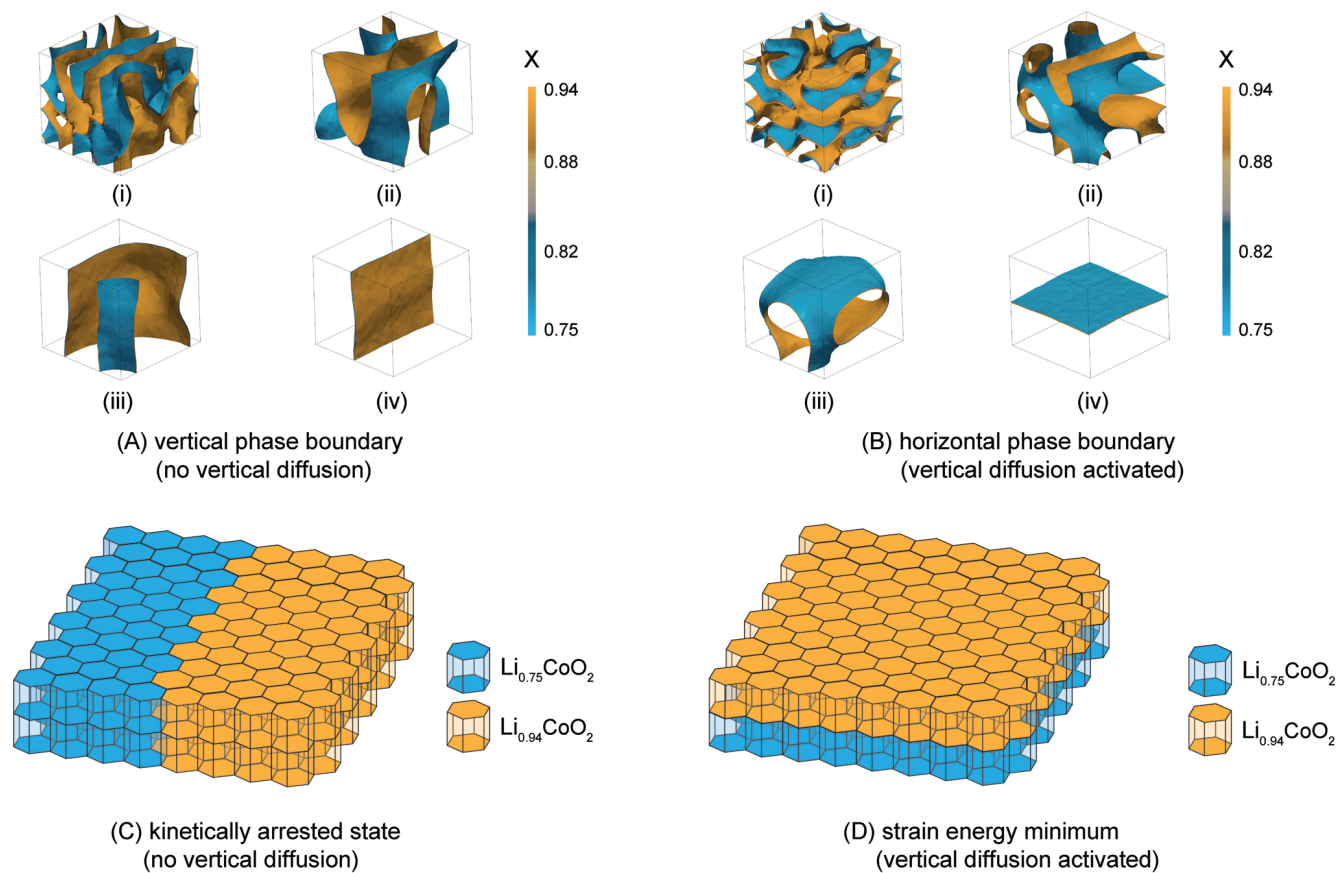


Figure 2. A) The contours (i)–(iv) show the evolution of the phase boundary over the course of the relaxation process of $\text{Li}_{0.85}\text{CoO}_2$. B) The contours (i)–(iv) show the evolution of the phase boundary over the course of the relaxation process of $\text{Li}_{0.85}\text{CoO}_2$, with an out-of-plane diffusion, caused due to the presence of defects such as Co^{4+} vacancies. C) The gold region depicts the Li-rich phase while the blue region represents the Li-poor phase. Equilibrium orientation of the phase boundary with in-plane diffusion. This leads to a kinetically arrested state which cannot be predicted by the minimization of strain energy. D) The gold region depict the Li-rich phase while the blue region represents the Li-poor phase. Equilibrium orientation of the phase boundary when the out-of-plane diffusion is activated. The phase boundary orientation is consistent with theoretical prediction using Hadamard's compatibility conditions.

and $v_2 = 1 - v_1$, respectively. On phase separation under zero traction, the orientation of the phase boundary is expected to be aligned such that the mechanical strain energy, produced by the misfit strain, is minimized. The misfit strain between the two phases is

$$\Delta\varepsilon_0 = \varepsilon_0(x_2) - \varepsilon_0(x_1) \quad (18)$$

Hadamard's Rank-1 compatibility conditions^[63] can be invoked to show that if $\Delta\varepsilon_0$ is of the form

$$\Delta\varepsilon_0 = \frac{1}{2}\alpha(\mathbf{a} \otimes \mathbf{n} + \mathbf{n} \otimes \mathbf{a}) \quad (19)$$

where α is an arbitrary constant, and \mathbf{a} and \mathbf{n} are unit vectors, then a configuration with the phase boundary oriented perpendicular to \mathbf{a} or \mathbf{n} will result in zero mechanical strain energy. In the case of LCO, it can be easily seen that

$$\mathbf{a} = \mathbf{n} = \hat{e}_c \quad (20)$$

satisfies this condition. Therefore, the theoretical equilibrium state should correspond to a phase-separated par-

ticle with the phase boundary aligned perpendicular to the c -axis.

To validate our theoretical predictions, we performed relaxation simulations on our nanoparticle. The simulations assume a uniform initial concentration of $x = 0.85$. The results for the phase boundary evolution for the nanoparticle are shown in **Figure 2B**. It can be seen from the contour plots shown in **Figure 2A**, that the relaxation does not produce the phase boundary as expected by the theory. This observation can be explained by the 2D basal in-plane diffusion mechanism of LCO, which leads to kinetically arrested states. Starting from a homogenous state, the only way to attain the theoretically predicted equilibrium state is via a diffusion-induced migration mechanism where the ions move across the layers through interlayer diffusion. However, this mechanism is not possible as only in-plane diffusion is allowed, in accordance with first-principles calculations.^[26] Therefore, the phase separation can occur only in-plane where each layer individually phase separates without any interlayer diffusion. This leads to a kinetically arrested state with a vertically aligned phase boundary.^[64]

To assess the accuracy of our hypothesis, we performed additional simulations with a small interlayer diffusion

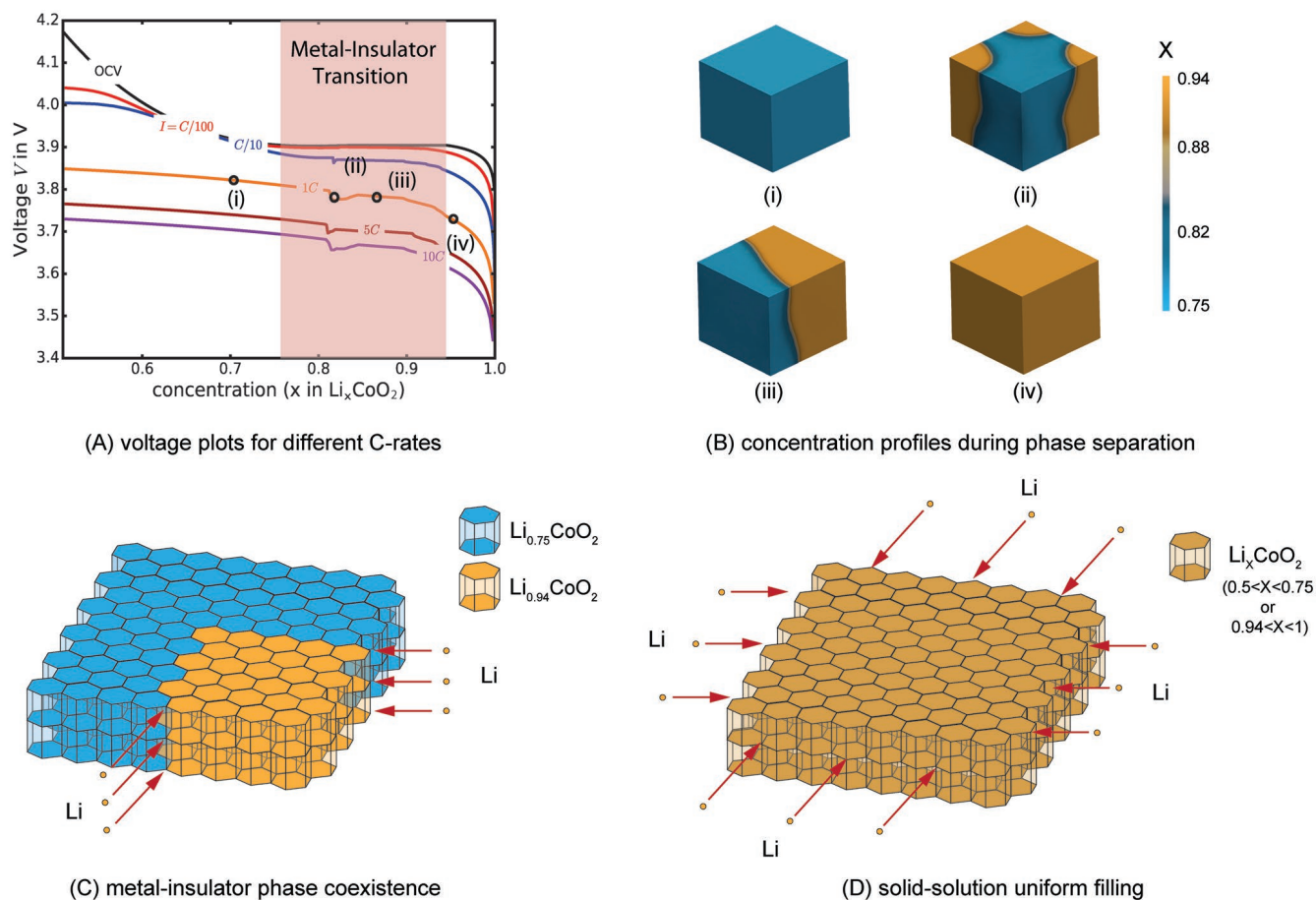


Figure 3. A) The voltage curves for different C-rates considering the reaction rate constant of the order $k_0 \approx 10^{-3} \text{ A m}^{-2}$. The transparent red box depicts the metal–insulator phase transition as observed in experiments. The small kinks represent the onset of phase transition at the spinodal points. B) The phase separation behavior observed in the metal–insulator transition region. C) The mechanism of ion insertion for the phase-separating metal-to-insulator transition region where the gold phase represents the lithium-rich phase while the blue region corresponds to the lithium-poor phase. The insertion, in this case, occurs in an ordered fashion only at the phase interface leading to the motion of the phase boundary. D) The mechanism of ion insertion for the solid solution region, where the filling takes place uniformly through all the side facets of the particle.

$D_c (\approx 10^{-5} D_a)$. In this case, we found that the particle does relax to the theoretically predicted equilibrium configuration. This shows that the in-plane diffusion does indeed produce kinetically arrested states, and also that defects such as interstitials and Co^{4+} vacancies leading to interlayer diffusion can cause the phase boundary to reorient itself to reach the theoretical minimum-energy configuration over long time scales. Further experimentation is necessary to determine if the defect-actuated out-of-plane diffusion mechanism is possible to drive the particle into its theoretically predicted energetic minimum.

3.2. Nonequilibrium Behavior at Different Discharging Rates

In order to explore the nonequilibrium behavior of LCO, we performed dynamic lithiation simulations at different discharging rates. Constant current simulations are conducted by prescribing the total current under the galvanostatic constraint, Equation (16). The discharge curves, obtained for different values of currents, I , are shown in **Figure 3A**. There are two specific mechanisms that come into play during the discharge

process, both shown in **Figure 3C,D**. At low concentrations of lithium content in Li_xCoO_2 , i.e., $x < 0.75$, the discharge process takes place through the formation of a solid solution, leading to an almost homogeneous filling throughout the particle. As the average concentration of lithium reaches the first spinodal point ($x \approx 0.75$), the solid solution phase separates through spinodal decomposition into the two phases viz. metallic phase ($x \approx 0.75$) and insulating ($x \approx 0.94$), **Figure 3B-ii**. The formation and growth of the instability manifests itself macroscopically through a sharp kink in the voltage curve, **Figure 3A**, similar to previously observed simulations in the Li_xFePO_4 cathode material.^[58] For all the simulated current values, the kinks are observed at the metallic-phase edge of the metal–insulator transition region, **Figure 3A**. After the onset of phase separation, the ion insertion occurs in an ordered way where the flux is concentrated at the phase boundary as a result of the non-vanishing interfacial curvature. The filling of Li ions proceeds through the motion of this phase boundary till every region in the particle reaches the insulating-phase edge ($x \approx 0.94$) of the metal–insulator transition region. It is important to note that the mechanism of filling is reminiscent of the reaction-limited

filling behavior as in the case of Li_xFePO_4 .^[51–53] This behavior can be explained through the small values of the Damköhler number that imply that diffusion dominates reactions at the nanoscale thereby giving rise to a flat phase boundary movement. For larger particles or large currents (leading to larger Damköhler numbers), the mechanism transitions to a diffusion-limited core–shell type (see the Supporting Information for more details). At the insulating-phase edge, the phase-separating behavior reverts back to solid-solution filling. The different phase profiles seen during the process of lithiation are identified in Figure 3B. As shown in Figure 3A, by increasing the current the resulting voltage decreases. This occurs as a result of the galvanostatic condition, Equation (16), which requires the establishment of larger overpotentials η in order to maintain the applied I . At higher currents, the voltage plateau no longer remains flat but shows a dip as the lithiation takes place. This tilting behavior is similar to the one observed in other nanoscale battery materials such as Li_xFePO_4 .^[51–53,58]

3.3. Modeling the Conductivity Changes across the Metal–Insulator Transition Regime

The nature of the metal–insulator transition in Li_xCoO_2 is still under debate in literature,^[13,25,65] due to the possibly coexisting effects of disorder induced localization^[66–68] and many-body correlations.^[69] These two mechanisms both lead to a metal–insulator transition,^[70] and can be induced by doping. The thermodynamic phase separation adds complexity to this problem, since no stable LCO phase with $0.75 < x < 0.94$ can be directly studied in the experiments, making it harder to decide if the transition is discrete or continuous. Multiple studies have proposed, mainly based on the very sharp decrease of conductance at $x > 0.94$, that this transition is a first-order metal–Mott insulator transition. Here, we adopt the picture of a Mott transition,^[69] and assume a 2D Hubbard model^[71–73] for the vacancy band created by delithiation. The Hubbard Hamiltonian is

$$H = \sum_{\langle i,j \rangle, s} -t_{ij} (c_{i,s}^\dagger c_{j,s} + \text{c.c.}) + \sum_i U \left(n_{i,+} - \frac{1}{2} \right) \left(n_{i,-} - \frac{1}{2} \right) \quad (21)$$

where $-t_{ij}$ is the nearest-neighbor hopping energy, U is the Hubbard electron interaction energy, $c_{i,s}$, $c_{i,s}^\dagger$, and $n_{i,\sigma}$ the hole annihilation, creation, and number density operators on site i , with s denoting spin degree of freedom.

The Green's function solution of the operator in Equation (21) can be given by the 2-pole approximation,^[74–76] qualitatively leading to a gap opening when electron correlation U/t is large. In the Hubbard band splitting picture, for $x < 0.94$ the density of states of the half-filled impurity band decreases continuously with increasing x . At the splitting concentration $x = 0.94$, a band gap opens and the conductance is exponentially dominated by the width of the gap. To first order, the gap depends linearly on the normalized Hubbard interaction $\Delta E \sim U/t$.^[69] Figure 4A illustrates the theoretical predictions of

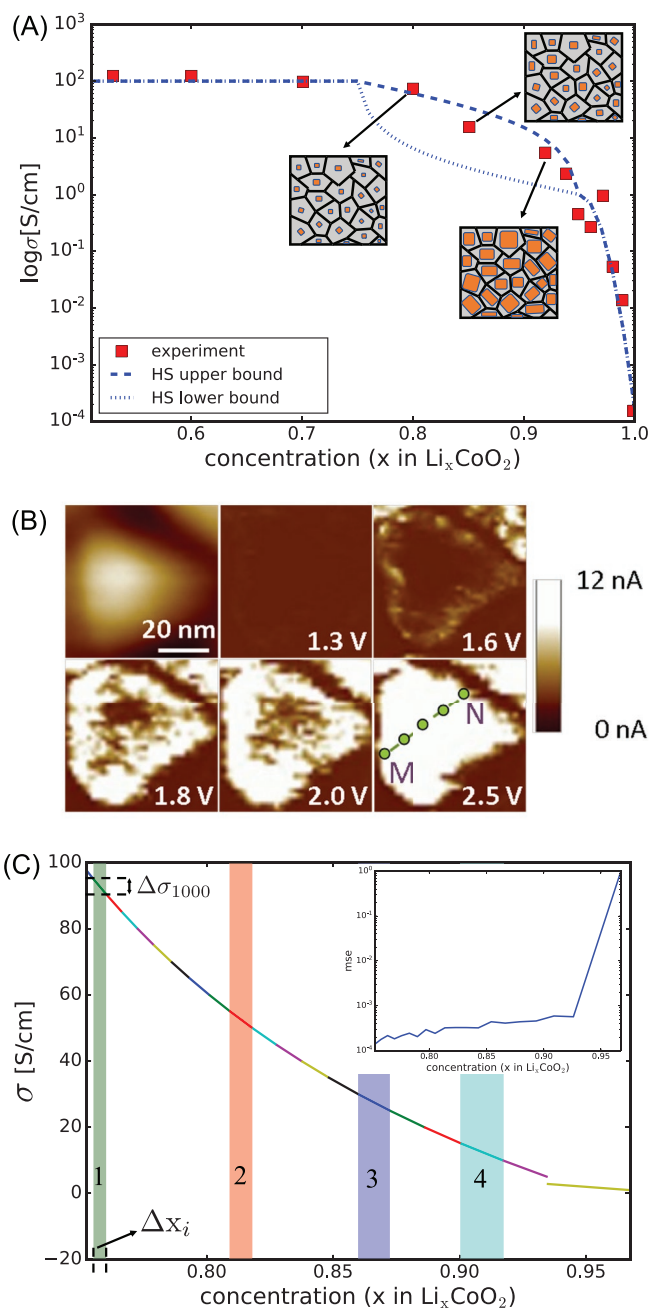


Figure 4. A) The conductance values from Milewska et al.^[25] are plotted along with the theoretical predictions. The Hashin–Shtrikman upper bound quantitatively captures the trend in the two-phase region. B) Local conductivity measurements by Zhu et al.^[79] show the evolution of lithium concentration in individual nanograins. The lithium gets extracted from the grain boundary creating an insulating core. The experiments therefore indicate the formation of a metallic percolating path (HS upper bound). C) Method outlining how the conductivity variation can be effectively utilized for creating different states for a memristive device. Blocks of linearized regimes are created where the conductance will vary approximately linearly with ion insertion over the region of interest. The inset in the figure shows the mean square error residual from a linear variation of the different regions of the conductance profile.

the proposed model for $x \in [0.5, 1]$. In the region $x > 0.94$, t/U admits the power law scaling $t/U \sim \Delta E^{-1} = C^{-1}(0.06 - n_{\text{hole}})^{-\alpha}$, with $n_{\text{hole}} = 1 - x$. Also, at $x = 0.94$ and $x = 1$ the interaction

energy is found to be 0 and 0.2 eV, respectively. In principle, the doping due to delithiation distorts the band and changes the charge carrier density of states.^[25] Here we assume that this disorder effect is negligible and we keep only an Arrhenius dependence on the electrical conductivity $\sigma \sim \sigma_0 \exp\left(-\frac{\Delta E}{k_B T}\right)$.

The parameters are $\sigma_0 = 1 \text{ S cm}^{-1}$ and $C = 55.56 \text{ eV}$, while the best fit is obtained for $\alpha = 2$. During phase separation, in the limit of mixing crystallites of different sizes and orientations, the macroscopic conductance can safely be assumed isotropic, Figure 4A. The polycrystalline material can then be modeled by rank- d laminates,^[77] which recovers the d -dimensional Hashin–Shtrikman (HS) bounds^[78]

$$\langle \sigma \rangle - \frac{(\sigma_1 - \sigma_2)^2 \phi(1 - \phi)}{\langle \bar{\sigma} \rangle + (d - 1)\sigma_2} \leq \bar{\sigma}_{\text{HS}} \leq \langle \sigma \rangle - \frac{(\sigma_1 - \sigma_2)^2 \phi(1 - \phi)}{\langle \bar{\sigma} \rangle + (d - 1)\sigma_1} \quad (22)$$

where $\langle \sigma \rangle = \sigma_1 \phi + \sigma_2(1 - \phi)$ and $\langle \bar{\sigma} \rangle = \sigma_2 \phi + \sigma_1(1 - \phi)$, σ_1 and σ_2 being the conductance of the conducting and insulating phases, respectively, ϕ the volume fraction of the conducting phase. The bounds are compared with the experimental data from Milewska et al.,^[25] Figure 4A. As can be observed, the data closely follow the HS upper bound suggesting that the conductive metallic phase percolates the insulating phase. In thin-film polycrystalline Li_xCoO_2 , it has been observed by Zhu et al. that the lithium is depleted along the grain boundaries for large grains ($\approx 100 \text{ nm}$), due to the lithium diffusion barrier being smaller at the grain boundaries.^[79] An experimental image of an individual nanograin showing this behavior is shown in Figure 4B where the lighter regions correspond to the metallic phase while the darker regions depict the insulating phase. In the experiments of Milewska et al., the average grain size was 300 nm. This indeed confirms the theory that the conductive metallic phase forms percolating paths across grains as shown in the insets in Figure 4A.

The phase coexistence region can be utilized effectively to build a memristive device, where the conductance $\sigma(q)$ (or resistance) is a function of the total state-of-charge q . Recent experiments^[27] successfully demonstrate the use of LCO as an effective memristor material. The modeling of a memristive device needs to be augmented by additional equations to account for electrostatic potential variations within the LCO channel. This is due to the injection of conduction electrons that indirectly affect the overpotential for ion-intercalation. For additional equations accounting for the extra physics, please refer to the Supporting Information. An ideal memristor should show linearity in the charge–conductance plot.^[80] This is to ensure that with every additional Δq insertion of Li ions, the resistance increases in linear steps, with each step change corresponding to a single memristive “state.” Additionally, for a given current input, as $\Delta q = I\Delta t$, for faster switching speed (i.e., small Δt), a large $d\sigma/dq$ slope is ideal, in order to pack large number of states for small changes in q .^[80] Therefore, given the inverse conductance profile, $q(\sigma)$ and total conductivity change $\Delta\sigma$, the residual

$$R(\sigma; \alpha, \beta) = \int_{q(\sigma)}^{q(\sigma + \Delta\sigma)} [q(s) - \alpha s - \beta]^2 ds \quad (23)$$

needs to be minimized for near-linear operating conditions and α should be large. Here, α and β are the linearizing parameters. Assuming over a typical size of $1 \mu\text{m}$ LCO material, each state differs by $\delta\sigma \approx 5 \text{ nS}$,^[27] the total region over which linearity needs to be maintained is $\Delta\sigma = 1000 \delta\sigma$. In Figure 4C, we outline a method to effectively design a linear region for a memristor with 1000 states for the current experiment. We find that Region 1 in Figure 4C corresponds to a low residual value and a large $d\sigma/dq$ which satisfies both the conditions, and therefore can be used for efficient memristor operation. We envision that a similar design strategy can be employed for different memristor materials, given their conductance profile.

4. Conclusions

We have developed an electro-chemomechanical model for Li_xCoO_2 for the range of operation of $0.5 < x < 1$ which accounts for the thermodynamics of phase separation due to the metal–insulator transition and mechanical strain energy due to lattice expansion, coupled with thermodynamically consistent ion-insertion reaction kinetics.

Our simulations on equilibrium relaxations in the phase coexistence regime predict the generation of a kinetically arrested state that is different from the thermodynamic energetic minimum. The formation of this configuration can be explained by the 2D in-plane diffusion which does not allow ion transport across the layers of Li_xCoO_2 . The smallest amount of interlayer diffusion, e.g. through defects such as Co^{4+} vacancies and interstitials, permits the phase evolution into a configuration that minimizes the strain energy. Further experimentation is necessary to ascertain the possibility of such a phase behavior.

Based on the generalized Butler–Volmer reaction kinetics, we capture the voltage plateau due to coexistence as observed in experiments and determine voltage behavior for different reaction rates. The reaction proceeds through the formation of a surface reaction-limited intercalation wave at the nanoscale. For larger currents or particle sizes (i.e., smaller Damköhler numbers), the filling behavior transitions to a diffusion-limited shrinking core type. A careful analysis on determining the critical Damköhler number for this transition will be reported in subsequent studies.

In addition, we capture the conductivity changes in an Li_xCoO_2 polycrystalline thin film through the modeling of three separate regimes: i) for low lithium concentrations, the conductivity of the metallic phase is assumed to be constant, ii) the conductivity of the metal–insulator phase coexisting region is captured by the Hashin–Shtrikman upper bound, and iii) the insulator regime is calculated using a Hubbard model for vacancy band generation due to delithiation. Finally, we suggest a strategy for identifying the region over which memristive computations can be performed by minimizing a linear residual. We envision that this model, coupled with the conductivity calculations, can be used for device-level modeling of Li_xCoO_2 -based low voltage memristors as well as in multiphase porous electrode theory (MPET) for battery simulations.

Supporting Information

Supporting Information is available from the Wiley Online Library or from the author.

Acknowledgements

This work was supported by the Toyota Research Institute program on Accelerated Materials Design and Discovery through D3BATT: Center for Data-Driven Design of Li-Ion Batteries.

Conflict of Interest

The authors declare no conflict of interest.

Keywords

energy materials, energy storage, information storage, Li-ion batteries, metal–insulator transition, neuromorphic computing devices

Received: April 7, 2019

Revised: July 2, 2019

Published online: August 9, 2019

- [1] T. Placke, R. Kloepsch, S. Dühnen, M. Winter, *J. Solid State Electrochem.* **2017**, *21*, 1939.
- [2] G. Crabtree, E. Kocs, L. Trahey, *MRS Bull.* **2015**, *40*, 1067.
- [3] K. Mizushima, P. Jones, P. Wiseman, J. B. Goodenough, *Mater. Res. Bull.* **1980**, *15*, 783.
- [4] K. Mizushima, P. Jones, P. Wiseman, J. Goodenough, *Solid State Ionics* **1981**, *3*, 171.
- [5] C. Wolverton, A. Zunger, *Phys. Rev. Lett.* **1998**, *81*, 606.
- [6] F. Ning, S. Li, B. Xu, C. Ouyang, *Solid State Ionics* **2014**, *263*, 46.
- [7] H. Moriwake, A. Kuwabara, C. A. Fisher, R. Huang, T. Hitosugi, Y. H. Ikuhara, H. Oki, Y. Ikuhara, *Adv. Mater.* **2013**, *25*, 618.
- [8] A. Van der Ven, M. Aydinol, G. Ceder, G. Kresse, J. Hafner, *Phys. Rev. B* **1998**, *58*, 2975.
- [9] D. Carlier, A. Van der Ven, C. Delmas, G. Ceder, *Chem. Mater.* **2003**, *15*, 2651.
- [10] A. Van der Ven, G. Ceder, *Phys. Rev. B* **1999**, *59*, 742.
- [11] D. Kramer, G. Ceder, *Chem. Mater.* **2009**, *21*, 3799.
- [12] A. Van der Ven, M. K. Aydinol, G. Ceder, *J. Electrochem. Soc.* **1998**, *145*, 2149.
- [13] J. N. Reimers, J. Dahn, *J. Electrochem. Soc.* **1992**, *139*, 2091.
- [14] E. Rossen, J. Reimers, J. Dahn, *Solid State Ionics* **1993**, *62*, 53.
- [15] H. Wang, Y.-I. Jang, B. Huang, D. R. Sadoway, Y.-M. Chiang, *J. Electrochem. Soc.* **1999**, *146*, 473.
- [16] Y. S. Jung, A. S. Cavanagh, A. C. Dillon, M. D. Groner, S. M. George, S.-H. Lee, *J. Electrochem. Soc.* **2010**, *157*, A75.
- [17] Z. Chen, J. Dahn, *Electrochim. Acta* **2004**, *49*, 1079.
- [18] K. Zhao, M. Pharr, J. J. Vlassak, Z. Suo, *J. Appl. Phys.* **2010**, *108*, 073517.
- [19] M. Ménétrier, I. Saadoun, S. Levasseur, C. Delmas, *J. Mater. Chem.* **1999**, *9*, 1135.
- [20] Y. Shao-Horn, L. Croguennec, C. Delmas, E. C. Nelson, M. A. O'Keefe, *Nat. Mater.* **2003**, *2*, 464.
- [21] S. Levasseur, M. Menetrier, E. Suard, C. Delmas, *Solid State Ionics* **2000**, *128*, 11.
- [22] Y.-I. Jang, B. J. Neudecker, N. J. Dudney, *Electrochem. Solid-State Lett.* **2001**, *4*, A74.
- [23] H. Xia, L. Lu, G. Ceder, *J. Power Sources* **2006**, *159*, 1422.
- [24] Y. Shao-Horn, S. Levasseur, F. Weill, C. Delmas, *J. Electrochem. Soc.* **2003**, *150*, A366.
- [25] A. Milewska, K. Świerczek, J. Tobola, F. Boudoier, Y. Hu, D. Bora, B. Mun, A. Braun, J. Molenda, *Solid State Ionics* **2014**, *263*, 110.
- [26] A. Van der Ven, G. Ceder, *Electrochem. Solid-State Lett.* **2000**, *3*, 301.
- [27] E. J. Fuller, F. E. Gabaly, F. Léonard, S. Agarwal, S. J. Plimpton, R. B. Jacobs-Gedrim, C. D. James, M. J. Marinella, A. A. Talin, *Adv. Mater.* **2016**, *29*.
- [28] G. Indiveri, B. Linares-Barranco, R. Legenstein, G. Deligeorgis, T. Prodromakis, *Nanotechnology* **2013**, *24*, 384010.
- [29] M. Chu, B. Kim, S. Park, H. Hwang, M. Jeon, B. H. Lee, B.-G. Lee, *IEEE Trans. Ind. Electron.* **2015**, *62*, 2410.
- [30] S. Park, M. Chu, J. Kim, J. Noh, M. Jeon, B. H. Lee, H. Hwang, B. Lee, B.-g. Lee, *Sci. Rep.* **2015**, *5*, 10123.
- [31] M. A. Zidan, J. P. Strachan, W. D. Lu, *Nat. Electron.* **2018**, *1*, 22.
- [32] C. Yakopcic, T. M. Taha, G. Subramanyam, R. E. Pino, in *The 2013 Int. Joint Conf. on Neural Networks (IJCNN)*, IEEE, Dallas, TX, USA **2013**, pp. 1–7.
- [33] R. Hasan, T. M. Taha, C. Yakopcic, D. J. Mountain, in *IEEE Int. Conf. on Rebooting Computing (ICRC)*, IEEE, San Diego, CA, USA **2016**, pp. 1–8.
- [34] L. Chua, *IEEE Trans. Circuit Theory* **1971**, *18*, 507.
- [35] S. Lai, in *IEEE Int. Electron Devices Meeting, 2003 (IEDM'03), Technical Digest*. IEEE, Washington DC, USA **2003**, pp. 10–1.
- [36] H.-S. P. Wong, S. Raoux, S. Kim, J. Liang, J. P. Reifenberg, B. Rajendran, M. Asheghi, K. E. Goodson, *Proc. IEEE* **2010**, *98*, 2201.
- [37] B. C. Lee, E. Ipek, O. Mutlu, D. Burger, *ACM SIGARCH Computer Architecture News*, Vol. 37, ACM, Austin, TX, USA **2009**, pp. 2–13.
- [38] M. Prezioso, F. Merrih-Bayat, B. Hoskins, G. Adam, K. K. Likharev, D. B. Strukov, *Nature* **2015**, *521*, 61.
- [39] X. Guo, F. Merrih-Bayat, L. Gao, B. D. Hoskins, F. Alibart, B. Linares-Barranco, L. Theogarajan, C. Teuscher, D. B. Strukov, *Front. Neurosci.* **2015**, *9*, 488.
- [40] J. J. Yang, D. B. Strukov, D. R. Stewart, *Nat. Nanotechnol.* **2013**, *8*, 13.
- [41] G. W. Burr, R. M. Shelby, S. Sidler, C. Di Nolfo, J. Jang, I. Boybat, R. S. Shenoy, P. Narayanan, K. Virwani, E. U. Giacometti, *IEEE Trans. Electron Devices* **2015**, *62*, 3498.
- [42] M. Kim, I. Baek, Y. Ha, S. J. Baik, J. Kim, D. Seong, S. Kim, Y. Kwon, C. Lim, H. Park, in *Electron Devices Meeting (IEDM), 2010 IEEE International*, IEEE, San Francisco, CA, USA **2010**, pp. 19–23.
- [43] Y. van de Burgt, E. Lubberman, E. J. Fuller, S. T. Keene, G. C. Faria, S. Agarwal, M. J. Marinella, A. A. Talin, A. Salleo, *Nat. Mater.* **2017**, *16*, 414.
- [44] E. J. Fuller, S. T. Keene, A. Melianas, Z. Wang, S. Agarwal, Y. Li, Y. Tuchman, C. D. James, M. J. Marinella, J. J. Yang, *Science* **2019**, *364*, 570.
- [45] X. Zhu, D. Li, X. Liang, W. D. Lu, *Nat. Mater.* **2019**, *18*, 141.
- [46] Q. Liu, Y. Liu, J. Li, C. Lau, F. Wu, A. Zhang, Z. Li, M. Chen, H. Fu, J. Draper, X. Cao, C. Zhou, *ACS Appl. Mater. Interfaces* **2019**, *11*, 16749.
- [47] S. Yamakawa, H. Yamasaki, T. Koyama, R. Asahi, *J. Power Sources* **2013**, *223*, 199.
- [48] V. Yurkiv, S. Sharifi-Asl, A. Ramasubramanian, R. Shahbazian-Yassar, F. Mashayek, *Comput. Mater. Sci.* **2017**, *140*, 299.
- [49] L. Wu, Y. Zhang, Y.-G. Jung, J. Zhang, *J. Power Sources* **2015**, *299*, 57.
- [50] S. Yamakawa, N. Nagasako, H. Yamasaki, T. Koyama, R. Asahi, *Solid State Ionics* **2018**, *319*, 209.
- [51] D. A. Cogswell, M. Z. Bazant, *ACS Nano* **2012**, *6*, 2215.
- [52] G. K. Singh, G. Ceder, M. Z. Bazant, *Electrochim. Acta* **2008**, *53*, 7599.
- [53] N. Nadkarni, E. Rejovitsky, D. Fraggadakis, C. V. Di Leo, R. B. Smith, P. Bai, M. Z. Bazant, *Phys. Rev. Mater.* **2018**, *2*, 085406.
- [54] N. J. de Klerk, A. Vasileiadis, R. B. Smith, M. Z. Bazant, M. Wagemaker, *Phys. Rev. Mater.* **2017**, *1*, 025404.

- [55] A. Vasileiadis, N. J. de Klerk, R. B. Smith, S. Ganapathy, P. P. R. Harks, M. Z. Bazant, M. Wagemaker, *Adv. Funct. Mater.* **2018**, *28*, 1705992.
- [56] R. B. Smith, M. Z. Bazant, *J. Electrochem. Soc.* **2017**, *164*, E3291.
- [57] T. R. Ferguson, M. Z. Bazant, *J. Electrochem. Soc.* **2012**, *159*, A1967.
- [58] P. Bai, D. A. Cogswell, M. Z. Bazant, *Nano Lett.* **2011**, *11*, 4890.
- [59] Y. Reynier, J. Graetz, T. Swan-Wood, P. Rez, R. Yazami, B. Fultz, *Phys. Rev. B* **2004**, *70*, 174304.
- [60] O. Redlich, A. Kister, *Ind. Eng. Chem.* **1948**, *40*, 345.
- [61] M. Z. Bazant, *Acc. Chem. Res.* **2013**, *46*, 1144.
- [62] D. Fraggedakis, J. Papaioannou, Y. Dimakopoulos, J. Tsamopoulos, *J. Comput. Phys.* **2017**, *344*, 127.
- [63] C. Truesdell, R. Toupin, *Principles of Classical Mechanics and Field Theory/Prinzipien der Klassischen Mechanik und Feldtheorie*, Springer, Berlin **1960**, pp. 226–858.
- [64] F. Hayee, T. C. Narayan, N. Nadkarni, A. Baldi, A. L. Koh, M. Z. Bazant, R. Sinclair, J. A. Dionne, *Nat. Commun.* **2018**, *9*, 1775.
- [65] C. A. Marianetti, G. Kotliar, G. Ceder, *Nat. Mater.* **2004**, *3*, 627.
- [66] P. W. Anderson, *Phys. Rev.* **1958**, *109*, 1492.
- [67] E. Abrahams, P. Anderson, D. Licciardello, T. Ramakrishnan, *Phys. Rev. Lett.* **1979**, *42*, 673.
- [68] F. Evers, A. D. Mirlin, *Rev. Mod. Phys.* **2008**, *80*, 1355.
- [69] F. Gebhard, *The Mott Metal-Insulator Transition*, Springer, Berlin **1997**.
- [70] K. Byczuk, W. Hofstetter, D. Vollhardt, *Phys. Rev. Lett.* **2005**, *94*, 056404.
- [71] J. Hubbard, *Proc. R. Soc. London, Ser. A* **1963**, *276*, 238.
- [72] J. Hubbard, *Proc. R. Soc. London, Ser. A* **1964**, *277*, 237.
- [73] J. Hubbard, *Proc. R. Soc. London, Ser. A* **1964**, *281*, 401.
- [74] L. M. Roth, *Phys. Rev.* **1969**, *184*, 451.
- [75] F. Mancini, S. Marra, H. Matsumoto, *Phys. C* **1995**, *244*, 49.
- [76] F. Mancini, S. Marra, H. Matsumoto, *Phys. C* **1995**, *250*, 184.
- [77] S. Torquato, *Random Heterogeneous Materials: Microstructure and Macroscopic Properties*, Vol. 16, Springer Science & Business Media, New York, NY **2013**.
- [78] Z. Hashin, S. Shtrikman, *CrossRef Google Scholar* **1963**.
- [79] X. Zhu, C. S. Ong, X. Xu, B. Hu, J. Shang, H. Yang, S. Katlakunta, Y. Liu, X. Chen, L. Pan, *Sci. Rep.* **2013**, *3*, 1084.
- [80] T. Gokmen, Y. Vlasov, *Front. Neurosci.* **2016**, *10*, 333.